Influence of Overlapping Tracks on Microstructure Evolution and Corrosion Behavior in Laser-melt Magnesium Alloy

Y. C. Guan [1a,b], W. Zhou [a b], Z.L. Li [b], H.Y. Zheng [b]

[a] Nanyang Technological University, 50 Nanyang Avenue, Singapore 639798

[b] Singapore Institute of Manufacturing Technology, 71 Nanyang Drive, Singapore 638075

Abstract:

Overlapping of laser beam tracks has significant influence on surface quality of laser-treated materials. This paper examines how overlapping tracks affect heat flow, solidification microstructure and electrochemical behavior of laser-melt magnesium alloy. Microstructure evolution of laser-melt surface with different overlapping rates at optimized scanning speed is investigated. Results show that solidification microstructure changes from cellular grains to cellular-dendritic and equiaxed dendritic in the overlapped area when overlapping rate increases. Numerical model suggests that Marangoni convection plays a predominate role in determining the solidification microstructure, and it increases significantly with the overlapping rate. The effect of microstructure in-homogeneities caused by overlapping on electrochemical behavior has also been analyzed.

Keywords: Laser; Overlapping; Solidification; Magnesium Alloy; Microstructure.

1. Introduction

Laser processing has recently generated intense research activities on improving surface properties of materials. Previous researchers have found that surface performance of metallic alloys, such as wear and corrosion resistance, is enhanced remarkably due to refined microstructure and enriched alloying elements following rapid solidification associated with the laser processing [1-9]. Mazumder and his co-works [4, 5] have investigated effect of laser-cladding technique upon the microstructure and the corrosion resistance of treated materials, and found that corrosion properties of the laser claddings has been improved significantly compared with that of commercially used materials. Gary and Luan [6] have reviewed various techniques for protective coatings on magnesium alloys due to poor surface properties, and suggested laser processing is a very promising method for Mg alloys to extend their industrial applications. Audebert *et al.* [7] have examined the ability of production of glassy metallic layers on Zr- and Mg-based alloys by laser surface treatment. Man *et al.* [8] have suggested that laser modification technique employed in their study is capable of enhancing the feasibility and biocompatibility of NiTi samples used as orthopedic implants mainly due to improved wear resistance. Most recently, Sun *et al.* [9] have studied laser surface alloying to form wear resistant layers on steel rolls with powders, and concluded that the improvement in wear resistance is attributed to combined results of grain refining and solution strengthening effect.

In order to apply laser techniques for large surface components in real engineering applications, overlapping adjacent traces as a result of multiple passes using scanning laser beam is usually necessary for production of area coverage. It has long been realized that laser beam overlapping may play a significant role in influencing the final surface properties of laser-treated materials [1-3]. Lewis and

[1] Corresponding author: Tel: (65) 6793 8386; Fax: (65) 6791 6377; E-mail: guan0013@e.ntu.edu.sg

Schlienger [10] have considered that overlapping plays an important role in determining quality control during laser assisted direct metal deposition. Particularly, overlapping is important in determining corrosion resistance due to microstructure in-homogeneities in the molten pool [11-16]. Liu *et al.* [11] have demonstrated that overlapping results in microstructural non-uniformity within re-heated and re-melted area, which leads to preferred sites for corrosion development. Reitz and Rawers [12] have observed that accelerated corrosion occurs near laser beam overlap region, and iron element segregated near periphery of each molten pool is responsible for accelerated corrosion in zirconium alloys. Virtanen *et al.* [13] have showed that pits are initiated along the overlapped area of laser traces after surface melting of Al-7Si and Al-12Si cast alloys. Conde *et al*. [14] have reported that corrosion resistance of laser-melt steels depends critically on laser processing parameters, and care must be taken in the choice of parameters that leads to optimal properties in each material. In our previous work, coarse structure of laser-melt AZ91D Mg alloy is investigated in the overlapped area caused by scanning speed, and it provides preferential site for pitting corrosion in simulated body fluid [15, 16].

However, as of now, there has been no concentrated effort to study the effect of laser beam overlapping on kinetics of solidification microstructure evolution in the molten pool. The objective of this research is to study how overlapping tracks affect heat transfer and liquid flow, microstructure evolution as well as electrochemical behavior of laser melting AZ91D Mg alloy at optimized scanning speed. The heat transport mechanism in the molten pool was analyzed from a well-tested numerical heat transfer and fluid flow model by DebRoy [17-19].

2. Materials and methods

The material studied was an as-cast AZ91D Mg alloy with the following chemical composition (wt. %): Al 8.97, Zn 0.78, Mn 0.31, Si 0.023, Cu 0.002, Ni 0.0005 and Mg balance. The specimens of 20 mm by 30 mm by 3 mm were extracted from the ingot, ground with progressively finer SiC paper (180, 400, 800, 1200, 2400 and 4000 grit), cleaned with alcohol, and then irradiated with Lumonics JK702 Nd:YAG laser system (with wavelength of 1064 nm) under high purity Ar gas protection. The fixed laser parameters were power density 3.82×10^4 W/cm^2, scanning speed 10 mm/s, frequency 100 Hz, and pulse duration 1 ms. Overlapping rate was varied from 25% to 90% during laser processing, as shown in Figure 1. Four specimens marked as E, F, G and H were chosen in this paper, as the overlapping rates were 25%, 50%, 75% and 90%, respectively. The laser was operated in a near TEM_{00} mode and the beam was defocused to 1 mm in diameter (the distance between two subsequent tracks was around 500 μm).

Microstructural features of the specimens were studied using a Zesis optical microscope, a JEOL 5600 LV SEM equipped with an energy-dispersive X-ray spectrometer (EDS), and JEOL 2010 TEM. The EDS measurements provided information on the chemical composition. The electrochemical behavior of as-received and laser-irradiated AZ91D specimens was studied using a potentiostat/galvanostat corrosion measurement system (EG&G model 263A) following procedures of ASTM: G59-97(2009) for Conducting Potentiodynamic Polarization Resistance Measurements [15]. The specimens were immersed in the 150 ml of 3.5% NaCl solution with a pH of 7.25. The exposed area was about 1 cm^2, and a polarization scan was carried out at a rate of 0.8 mV s^{-1}.

3. Results

Figure 2 and Figure 3 indicate top view of microstructure evolution at AZ91D Mg alloy surface before and after laser melting by SEM and TEM, respectively. As shown in Fig. 2(a), microstructure of as-received AZ91D Mg alloy contained bulk and lamellar β-$Mg_{17}Al_{12}$ phase distributed non-homogeneously in a matrix of α-Mg grains. After laser surface melting, solidification microstructure consisted of typical cellular/dendrite structure was observed in the molten pool, which was derived from refined α-Mg and β-$Mg_{17}Al_{12}$ phases according to previous study [15, 16]. Coarse structure was formed in the overlapped area along laser tracks, and the amount and size of such structure increased significantly with the laser overlapping rates, as shown in Fig. 2(b)-Fig. 2(e). These coarse structures were further investigated in Figure 2 shown as the high magnification images. At low overlapping rate, fine cellular structure with size of 2-3 μm were observed in the overlapped area, and small solidification cracks were also found in the microstructure, as shown in Fig. 2(b). When the overlapping rate increased from 25% to 75%, cellular structure to dendrite structure transition took place near solidification front at the periphery of each molten pool, and more dendrite was found in the overlapped area, as shown in Fig. 2(c) and Fig. 2(d). At high overlap rate as 90%, coarse equiaxed dendrite structure was formed, as shown in Fig. 2(e).

Quantitative analyses of chemical compositions based on EDS measurement found that with the increasing overlapping rates, average Al concentration in the overlapped area increased from 11.5 wt% to 16.7 wt%, whereas average Mg concentration decreased from 87.1 wt% to 82.2 wt% simultaneously. The reason for the chemical compositions change was due to enhanced selective vaporization of alloying elements with the increasing overlapping rates during laser processing [3, 15, 16].

Fig. 3(a) reveals thin plate shape of β-$Mg_{17}Al_{12}$ phase in the as-received surface. After laser melting, morphology of β-$Mg_{17}Al_{12}$ phase changed significantly to cellular/dendrite structure as well as nano-sized particles, as shown in Fig. 3(b)-(d). The evolution of these structures was in agreement of SEM observations. It should be noted that nano-sized particles were identified as β-$Mg_{17}Al_{12}$ precipitates according to further investigation of orientation relationship between the particles and α-Mg matrix. With the overlapping rate increases, a driving force tends to make dispersions of small crystals coarsening as a result of “quench-hold-quench” process [1, 16]. Correspondingly, tiny precipitates shrink and eventually vanish together, while large precipitates grow at their expense by solid-state diffusion during coarsening, leading to cluster-shaped particles in the microstructure. On the other hand, at 90% overlapping rate, strong selective vaporization of Mg and Al elements occurs due to accumulated high laser energy, resulting in Al enriched significantly in the laser- melt layer. The high density of enlarged and gathered particles as well as increased Al concentration would increase the volume fraction of brittle β-$Mg_{17}Al_{12}$ phase, the melt layer also becomes increasingly brittle [20]. Therefore, TEM result of specimen with 90% overlapping rate is missing because it was too brittle to break into pieces during sample preparation process.

Cross-section views of molten pool in the laser-melt specimens were investigated in Fig. 4 and Fig. 5. With the increasing overlapping rates, bottom morphology of the molten pool became flat, but melt depth kept as nearly 150 μm for all molten pools. Small solidification cracks were also found at low overlapping rate in the molten pool, as shown in Fig. 4(a). Further investigation was observed using SEM. At low overlapping rate, fine cellular structure was found in the end of previous laser trace, and needle-shape dendrite structure was formed along the laser trace, as shown in Fig. 5(a) and Fig. 5(b). Fig. 5(a) and Fig. 5(b) also show that few cellular/dendrite structures were found in the non-overlapped area of the molten pool. When overlapping rate was increased, coarse equiaxed dendritic structures replaced fine cellular and cellular-dendrite structure in the overlapped area, and the

solidification microstructure in the molten pool became much more homogenous, as shown in Fig. 5(c) and Fig. 5(d).

Polarization study of as-received material and laser-melt surfaces with different overlapping rates was further analyzed in 3.5% NaCl solution, as shown in Fig. 6. The values of corrosion potential (E_{corr}), Tafel slope (β_c) and corrosion current density (i_{corr}) for each polarization curve are summarized in Table 1, and the E_{corr} value of as-received AZ91D Mg alloy is in agreement with other researchers' finding [21, 22]. Fig. 6 shows that the E_{corr} values of laser-treated microstructures were shifted to less negative values, which indicating more cathodic behaviour compared with as-received microstructure. The cathodic part of the curve reveals that the cathodic currents were much lower for all laser irradiation specimens. The laser-melt microstructure was less active anodically with lower i_{corr} value compared with as-received material, resulting in improved corrosion resistance of AZ91D Mg alloy. Table 1 shows that the β_c values are similar for microstructures E and F (0.154 V and 0.113 V) or G and H (0.064 V and 0.078 V), indicating the same electrochemical reactions for E and F or for G and H. The difference in β_c value between E and F may be attributed to the cracks formed in the microstructure, as shown in Fig. 2 (b) and Fig. 4 (a). The difference in β_c value between G and H is attributed to the coarse structure formed in the overlapped area [15], as shown in Fig. 2 (c)-(e) and Fig. 5 (c)-(d).

4. Discussions

Microstructure development in the molten pool is complicated due to physical processes that occur during interaction of the heat source with the metal, including re-melting, heat and fluid flow, vaporization, dissolution of gasses, solidification, subsequent solid-state transformation, stresses, and distortion [17-19, 23]. These processes and their interactions profoundly affect rapid solidification and microstructure evolution. In situations where laser processing on metals, atoms move easily from liquid to solid and the interface moves quickly in response to very small undercooling [24]. Therefore, kinetics of rapid solidification is suggested to be heat-flow controlled rather than interface controlled [1-3, 24].

A numerical heat transfer and fluid flow model for molten pool has been extensively validated for various materials, and the detailed information is not repeated here [17-19]. The relative importance of convection and conduction in the overall transport of heat is evaluated from $P_e = U\sigma / \alpha_l$, where U is scanning speed of incident flux, σ is energy distribution parameter of incident flux, α_l is thermal diffusivity $\alpha_l = k/\rho C_\rho$ (k is thermal conductivity and C_ρ is specific heat). In this work, P_e increases significantly with the laser beam overlapping rates due to energy input σ when scanning speed U is optimized. Therefore, convection becomes dominant mechanism of heat transport in the molten pool.

Driving forces for liquid flow considered in the heat flow model include surface-tension and buoyancy forces [19]. The relative importance of buoyancy and surface-tension forces is determined from the ratio of surface-tension Reynolds number (M_a) to Grashof number (G_r)

$$R_{s/b} = \frac{M_a}{G_r} = \left(\frac{\rho L_R \Delta T \left| \partial\gamma / \partial T \right|}{\mu^2} \right) / \left(\frac{g\beta L_b^3 \Delta T \rho^2}{\mu^2} \right) = \frac{L_R \left| \partial\gamma / \partial T \right|}{g\beta L_b^3 \rho} \quad (1)$$

where ρ is the density of materials, g is gravitational acceleration, β is thermal expansion coefficient, L_R is characteristic length taken as the pool radius at the top surface of molten pool, L_b is characteristic

length for the buoyancy force in the liquid pool which is approximated by one eighth of the pool radius, μ is typical liquid velocity and $\partial\gamma/\partial T$ is temperature coefficient of surface tension, and ΔT is temperature difference between the peak pool temperature and solidus temperature. According to physical properties of AZ91D Mg alloy in the literature [25] and the measured molten pool radius 432 μm in Figure 4, the ratio of surface-tension force to buoyancy force was calculated as 4.07×10^5. Therefore, the liquid flow is driven mainly by the Marangoni flow.

Order of the maximal liquid velocity is approximated by

$$u_m^{3/2} \approx \frac{\partial\gamma}{\partial T}\frac{\partial\gamma}{\partial y}\frac{W^{1/2}}{0.664\rho^{1/2}\mu^{1/2}} \tag{2}$$

where $\partial\gamma/\partial y$ is the average temperature gradient in the molten pool, W is the molten pool radius and other variables have been defined before. With the increasing overlapping rates in current work, energy density delivered to the irradiated surface increases significantly due to the incident laser flux, leading to the average temperature gradient in the molten pool decreases [19]. Correspondingly, the maximal liquid velocity decreases according to Eq. (2), and surface tension force increases according to Eq. (1). Therefore, enhanced Marangoni convection effect occurs at high overlapping rate, resulting in homogenous microstructure in the molten pool, as shown in Fig. 2, Fig. 4 and Fig. 5. Moreover, the structure became coarse due to re-melted and re-solidification processes during laser irradiation [15, 16], as shown in Fig. 3, Fig. 5 and Fig. 6.

It is known that liquid-solid interface stability factor G (temperature gradient)/R (solidification rate) is related to morphology of solidification microstructure [26, 27]. The value of G/R decreases with the increasing overlapping rates according to governing equation of *G* and R based on the heat flow model [19]. As shown in Fig. 3 and Fig. 5, the fine cellular structure is found at low overlapping rate, the equiaxed-dendritic microstructure is formed at high overlapping rate and cellular-dendritic microstructure takes place in between. This is in agreement with previous study of solidification in the molten pool [18, 19]. Moreover, nanoscale β-$Mg_{17}Al_{12}$ particles enlarge and become globule with the increasing overlapping rates, in order to minimize the sum of interfacial and elastic interaction energies based on mechanisms of precipitates from supersaturation matrix [24, 28, 29]. However, it should be noted that the explanation presented here is given on qualitative basis for rapid solidification. Quantitative determination of microstructure evolution requires not only the parameter G/R, but also the thermodynamics and kinetics of solidification [30, 31]. Furthermore, the role of β-$Mg_{17}Al_{12}$ precipitates on electrochemical behavior of laser-melt surface is still not clear.

In addition, high tensile stresses occur when the specimens solidified and contracted unevenly at low overlapping rate due to large temperature gradient (G) [30]. Mg alloys have high thermal expansion coefficient as 16.1×10^{-6}/K between 20 and 400 °C, thereby the thermal stress at low overlapping rate are expected to be higher than that of high overlapping rate [16, 30, 32, 33]. Therefore, small cracks are formed in the solidification microstructure, and these cracks would accelerate the corrosion behavior of the laser-melt layer [4, 6], as shown in Fig.6 and Table 1.

5. Conclusions

Effect of overlapping tracks on solidification microstructure and electrochemical behavior of AZ91D Mg alloy was reported via irradiation by millisecond pulse Nd:YAG laser surface melting. The main conclusions are listed as following:

(1) With the increasing overlapping rates in laser-melt Mg alloy, morphology of solidification microstructure changed from cellular grains, to cellular-dendritic and equiaxed dendritic in the overlapped area of molten pool. Meanwhile, nano-sized β-$Mg_{17}Al_{12}$ precipitates grew and gathered as clusters under TEM observation.

(2) At high overlapping rate, enhanced Marangoni convection resulted in homogenous but coarse microstructure, and average Al concentration at the surface of laser-melt layer increased significantly due to heavy vaporization effect. At low overlapping rate, small solidification cracks were found in the microstructure due to high thermal stress.

(3) Electrochemical behavior of all laser-melt surfaces showed improved corrosion resistance with the same reactions, compared to as-received microstructure. However, the difference in value was attributed to coarse microstructure and solidification cracks in the molten pool.

Acknowledgements

Support by Nanyang Technological University, Ph.D. scholarship and Singapore Institute of Manufacturing Technology, A*STAR (Agency for Science, Technology and Research, Singapore), Collaborative Research Project U09-M-006SU is gratefully acknowledged.

References

1. Cunningham FE. The use of lasers for the production of surface alloys. Cambridge: Massachusetts Institute of Technology Press. 1964.
2. Peercy P. Laser Surface Treatment of Metals. Ed. by Draper C, Mazzoldi P. MA: Kluwer Academic Pulishers, Boston, 1986.
3. Steen WM. Laser industry: an Introduction to laser processing and its industrial application. Eds. J. Lawrence, J. Pou, D.K.Y. Low, E. Toyserkani. Advances in laser materials processing. Woodhead Publishing limited, CRC Press. 2010.
4. Wang AA, Sircar, S, Mazumder J. Laser cladding of Mg-Al alloys, J Mater Sci 1993; 28;5113-5122.
5. Mohanty PS, Mazumder J. Solidification behavior and microstructural evolution during laser beam-material interaction, Metall Mater Trans B 1998; 29; 1269-1279.
6. Gray JE, Luan B. Protective coatings on magnesium and its alloys-a critical review, J Alloys Comp 2002: 336; 88-113.
7. Audebert F, Colaco R, Vilar R, Sirkin H. Production of glassy metallic layers by laser surface treatment, Scr Mater 2003; 48; 281-286.
8. Man HC, Zhang S, Cheng FT, Guo X. In situ formation of a TiN/Ti metal matrix composite gradient coating on NiTi by laser cladding and nitriding. Surf Coat Technol 2006; 200; 4961-4966.
9. Sun GF, Zhang YK, Liu CS, Luo KY, Tao XQ, Li P. Microstructure and wear resistance enhancement of cast steel rolls by laser surface alloying NiCr-Cr_3C_2. Mater Des 2010;31; 2737-2744.
10. Lewis GK, Schlienger E. Practical considerations and capabilities for laser assisted direct metal deposition. Mater Des 2000; 21; 417-23.
11. Watkins KG, Liu Z, McMahon M, Vilar R, Ferreira MGS. Influence of the overlapped area on the corrosion behaviour of laser treated aluminium alloys. Mater Sci Eng A 1998; 252; 292-300.
12. Reitz W, Rawers J. Effect of laser surface melted Zirconium alloys on microstructure and

corrosion-resistance. J Mater Sci 1992; 27; 2437-43.
13. Virtanen S, Bohni H, Busin R, Marchione T, Pierantoni M, Blank E. The effect of laser-surface modification on the corrosion behavior of Fe and Al base alloys. Corr Sci 1994; 36; 1625-44.
14. Conde A, Colaco R, Vilar R, de Damborenea J. Corrosion behaviour of steels after laser surface melting. Mater Des 2000; 21; 441-5.
15. Guan YC, Zhou W, Zheng HY. Effect of Laser Surface Melting on Corrosion Behaviour of AZ91D in Simulated-modified Body Fluid. J Appl Electrochem 2009; 39; 1457-64.
16. Guan YC, Zhou W, Zheng HY, Li. ZL. Solidification Microstructure of AZ91D Mg Alloy after Laser Surface Melting. Appl Phys A 2010; 101; 339-44.
17. Yang Z, DebRoy T. Modeling macro-and microstructures of gas-metal-arc welded HSLA-100 steel. Metall Mater Trans B 1999; 30; 483-93.
18. Mishra S, DebRoy T. Measurements and Monte Carlo simulation of grain growth in the heat-affected zone of Ti-6Al-4V welds. Acta Mater 2004; 52; 1183-92.
19. He X, Elmer JW, DebRoy T. Heat transfer and fluid flow in laser microwelding. J Appl Phys 2005; 97; 084909.
20. Per B, Ketil P, Håkon W. Improving the Strength and Ductility of Magnesium Die-Casting Alloys via Rare-Earth Addition, JOM, 2003; 46-51.
21. Ambat R, Aung NN, Zhou W. Studies on the influence of chloride ion and pH on the corrosion and electrochemical behaviour of AZ91D magnesium alloy. J Appl Electrochem 2000; 30;865-74.
22. Pardo A, Merino MC, Coy AE, Arrabal R, Viejo F, Matykina E. Corrosion behaviour of magnesium/aluminium alloys in 3.5 wt.% NaCl. Corr Sci 2008; 50; 823-34.
23. David SA, Babu SS, Vitek JM. Welding: Solidification and Microstructure. JOM 2003; 55; 14-20.
24. Stefanescu DM, Ruxanda R. Fundamentals of Solidification. ASM Handbook, ASM International, Materials Park, OH, 2004.
25. Erickson SC. Magnesium in Properties and Selection: Nonferrous Alloys and Special-Purpose Materials, ASM Handbook, ASM International, Materials Park, Ohio, 2002.
26. Kou S. Welding Metallurgy, Wiley, New York, 2002.
27. Liu WP, DuPont JN. Effects of melt-pool geometry on crystal growth and microstructure development in laser surface-melted superalloy single crystals. Mathematical modeling of single-crystal growth in a melt pool (part I). Acta Mater 2004; 52; 4833-47.
28. Banerjee R, Genc A, Hill D, Collins PC, Fraser HL. Nanoscale TiB precipitates in laser deposited Ti-matrix composites. Scr Mater 2005;53;1433-7.
29. Lin X, Yue TM. Phase formation and microstructure evolution in laser rapid forming of graded SS316L/Rene88DT alloy. Mater Sci Eng A, 2005; 402; 294-306.
30. Nayak S, Wang H, Dahotre NB. Thermography during laser surface melting of cast aluminium alloy. Mater Sci Techno 2004; 20; 1609-14.
31. DebRoy T, David SA. Physical processes in fusion-welding. Rev Mod Phys 1995; 67; 85-112.
32. Zhou W, Long TZ, Mark CK. Hot cracking in tungsten inert gas welding of magnesium alloy AZ91D. Mater Sci Tech 2007; 23; 1294-9.
33. Qua HP, Li P, Zhang SQ, Li A, Wang HM. The effects of heat treatment on the microstructure and mechanical property of laser melting deposition c-TiAl intermetallic alloys. Mater Des 2010; 31; 2201-10.

Figure captions

Fig. 1 Schematic diagram of laser surface melting process

Fig. 2 Scanning electron micrographs showing top view of microstructure evolution at AZ91D Mg alloy surface before and after laser melting with increasing overlapping rate: (a) as-received alloy; (b) E; (c) F; (d) G and (e) H. High magnification images from the areas were also shown.

Fig. 3 Transmission electron microscopy showing solidification microstructure in AZ91D Mg alloy before and after laser melting with increasing overlapping rate: (a) as-received alloy; (b) E; (c) F; (d) G. SAD pattern from one of these particles exhibiting β-$Mg_{17}Al_{12}$ structure.

Fig. 4 Cross-section views of the irradiated AZ91D Mg alloy with increasing overlap rates (a) E (b) F (c) G and (d) H.

Fig. 5 Scanning electron micrographs showing cross-section views of solidification microstructure in laser-melt AZ91D Mg alloy with increasing overlapping rates: (a) E (b) F (c) G and (d) H. High magnification images from the areas were also shown.

Fig. 6 Potentiodynamic polarisation curves for AZ91D Mg alloy before and after laser irradiation in 3.5% NaCl solution.

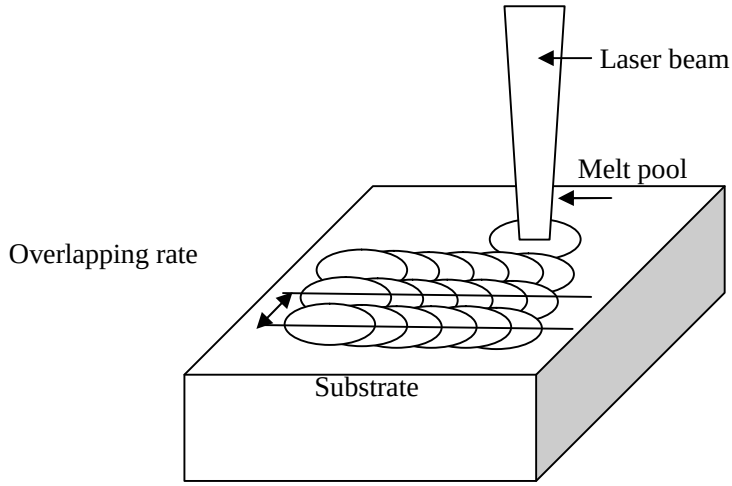

Fig. 1

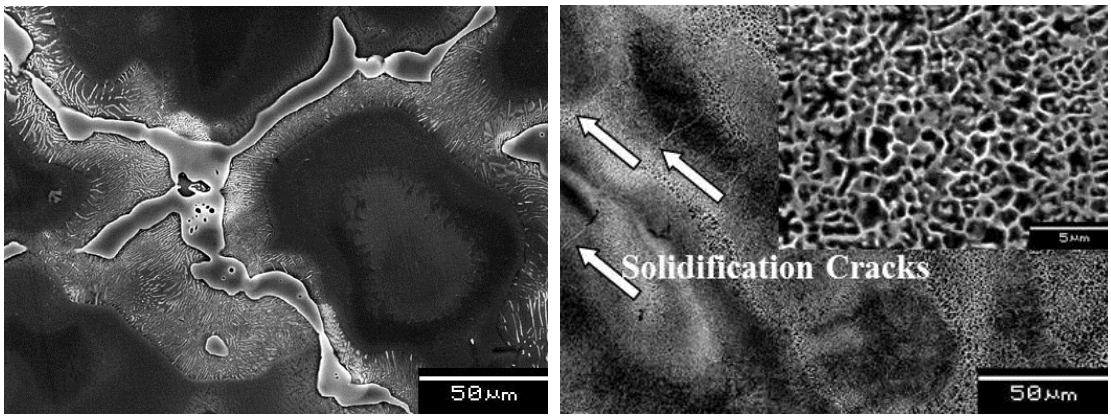

(a) (b)

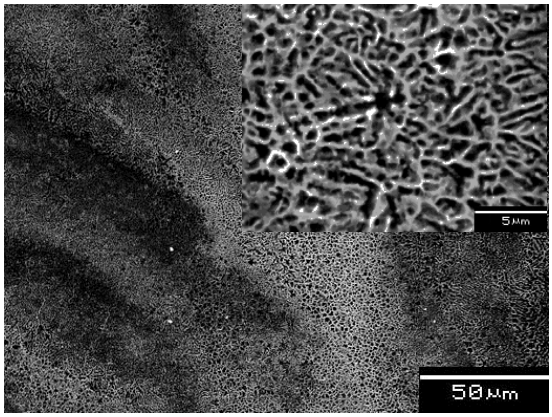

(c)

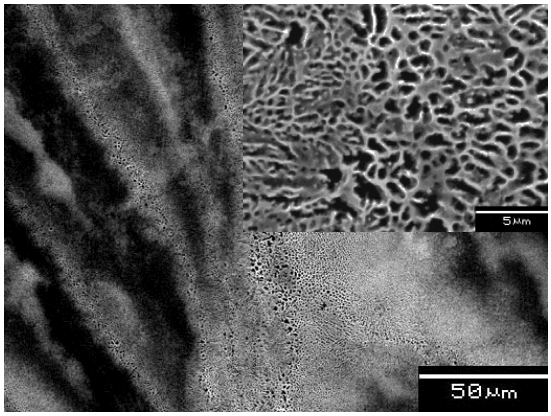

(d)

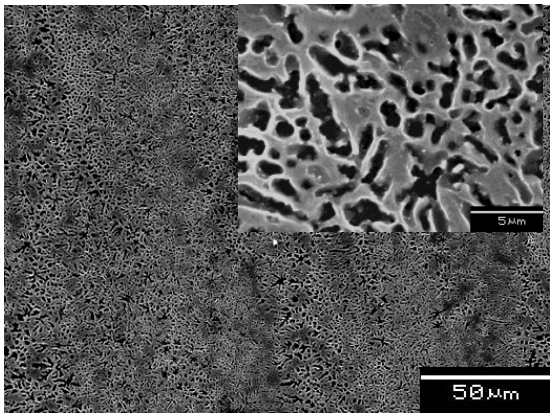

(e)

Fig. 2

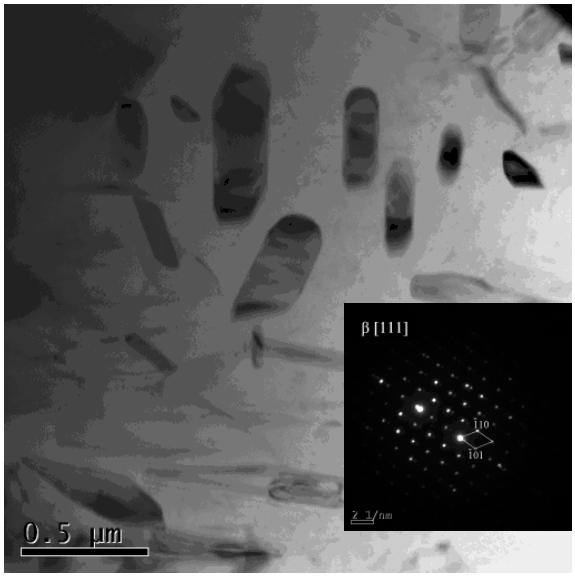

(a)

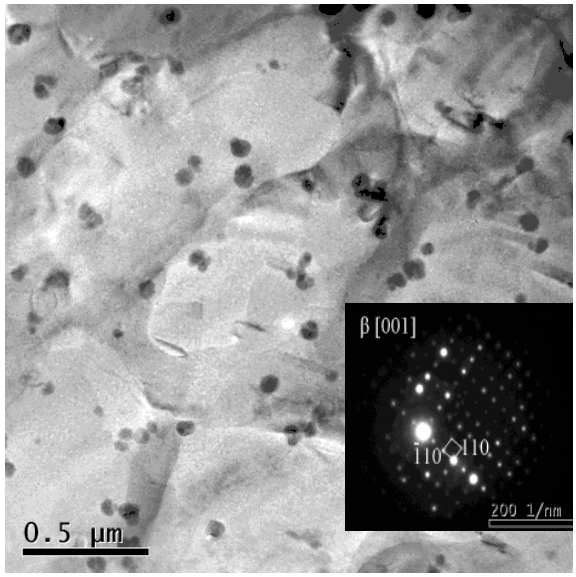

(b)

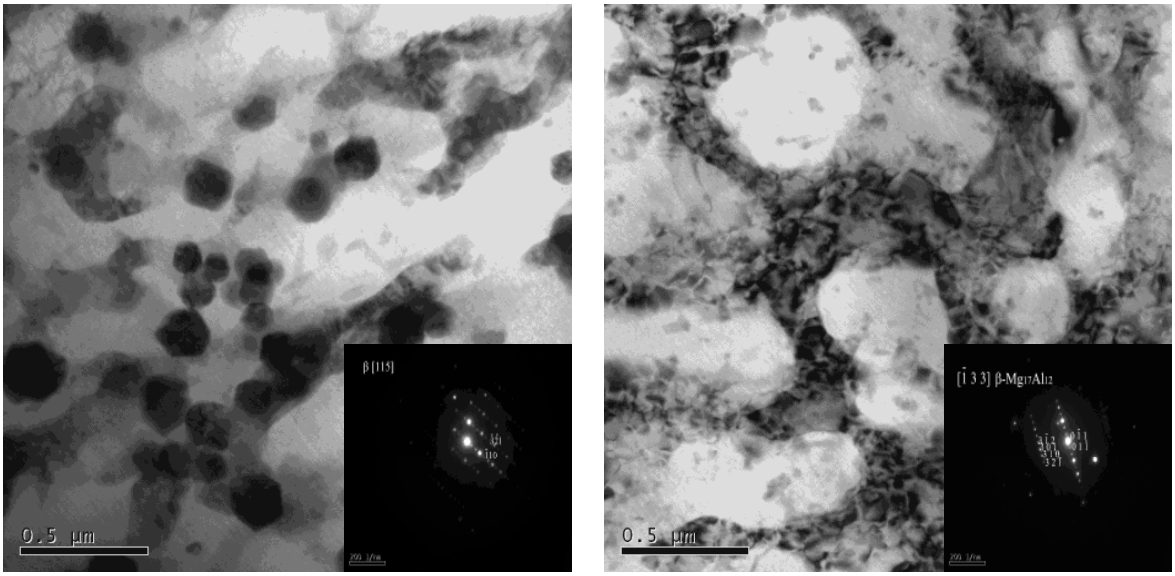

(c) (d)

Fig. 3

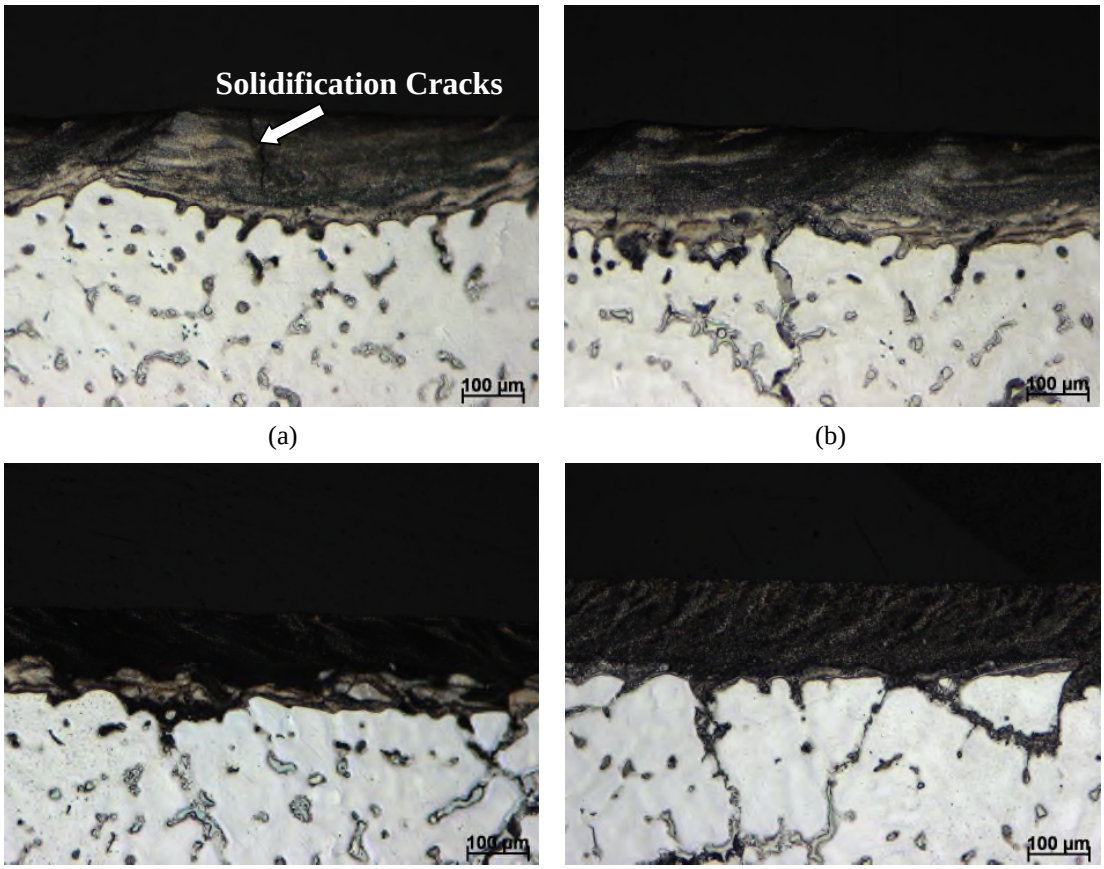

(a) (b)

(c) (d)

Fig. 4

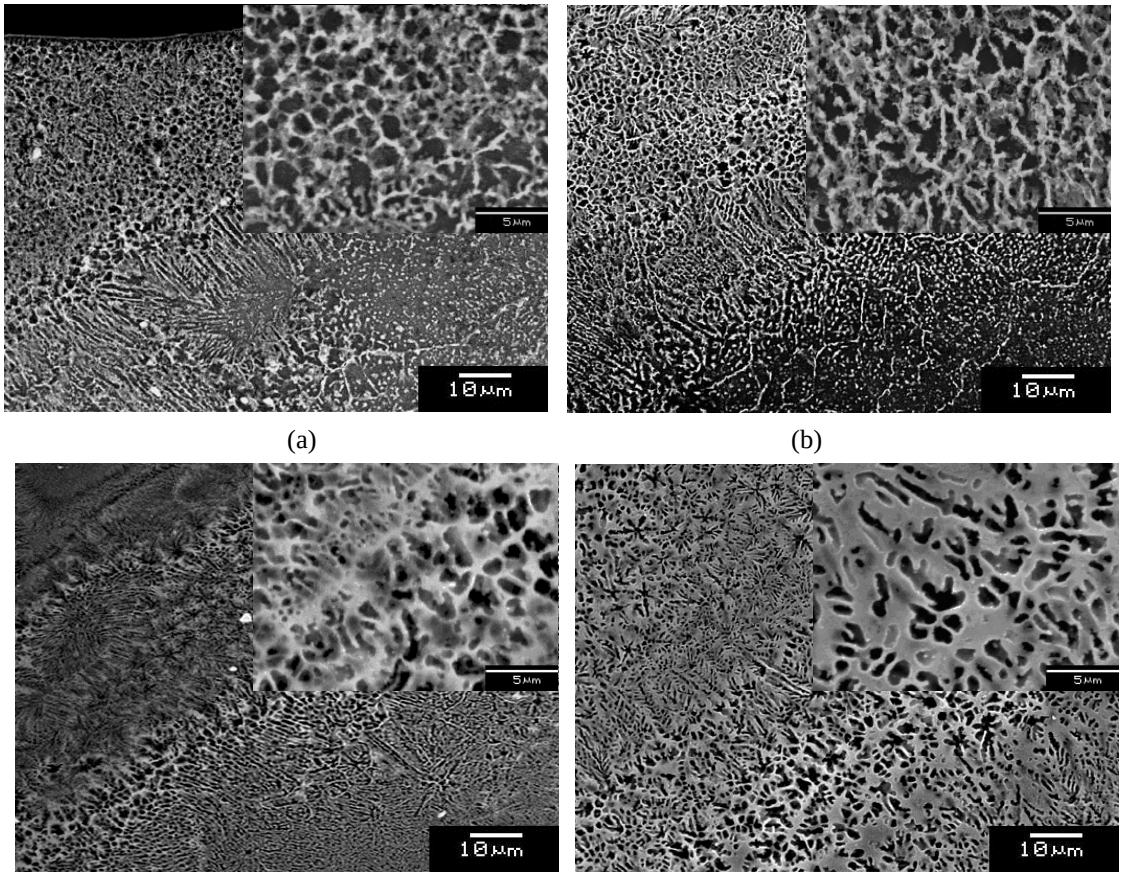
5μm
10μm
(a)
(b)
(c)
(d)

Fig. 5

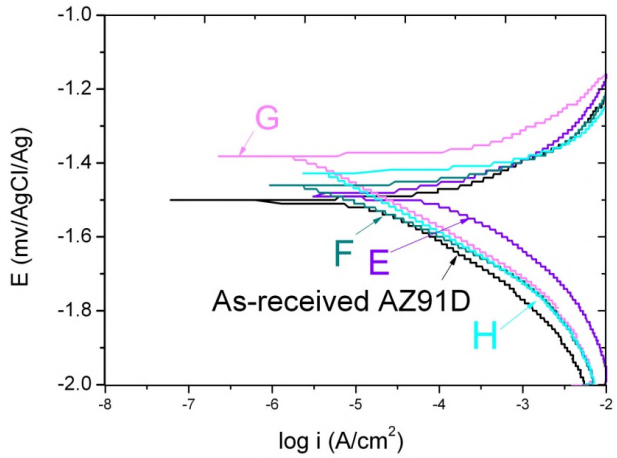
-1.0
-1.2
-1.4
-1.6
-1.8
-2.0
-8
-7
-6
-5
-4
-3
-2
E (mv/AgCl/Ag)
log i (A/cm2)
G
F
E
H
As-received AZ91D

Fig. 6

Table

Table 1 E_{corr}, β_c and I_{corr} values for AZ91D alloy before and after laser irradiation in 3.5% NaCl solution

Specimens	E_{corr} (V)	β_c (V)	I_{corr} (mA/cm^2)
As-received	-1.504	0.184	0.016
E	-1.488	0.154	0.012
F	-1.459	0.113	0.010
G	-1.382	0.064	0.005
H	-1.425	0.078	0.008